Electronic Supplementary Information (ESI)

Oxidative nucleation and growth of Janus-type MnO_x-Ag and MnO_x-AgI nanoparticles

Lei Zhang,[a,b] Lei Jin,[b] Yue Yang,[b,d] Xingsong Su, [a,b] Peter Kerns,[b] Michael Meng,[b] Ben Liu [a,*] and Jie He [b,c,*]

[a]Jiangsu Key Laboratory of New Power Batteries, Collaborative Innovation Center of Biomedical Functional Materials, School of Chemistry and Materials Science, Nanjing Normal University, Nanjing 210023, China
[b]Department of Chemistry, University of Connecticut, Storrs, Connecticut 06269, USA
[c]Polymer Program, Institute of Materials Science, University of Connecticut, Storrs, Connecticut 06269, USA
[d]Department of Chemical Engineering, Nanjing University of Science and Technology, Jiangsu 210094, China

Table S1. The summary of peak position obtained from the deconvoluted Mn 2p, Mn 3s, Ag 3d and I 3d XPS spectra of the initial MnO octahedrons, Janus MnO_x-Ag and MnO_x-AgI NPs.

Sample	Peak Position / eV						
	$Mn2P_{1/2}$	$Mn2P_{3/2}$	△Mn 3S	$Ag\ 3d_{3/2}$	$Ag\ 3d_{5/2}$	$I\ 3d_{3/2}$	$I\ 3d_{5/2}$
MnO	652.5	640.8	5.9	/	/	/	/
MnOx-Ag	652.6	641.4	5.3	373.8	367.8	/	/
MnOx-AgI	653.3	641.5	5.1	373.5	367.5	630.5	619

Table S2. The percentage of Mn^{2+}, Mn^{3+} and Mn^{4+} in the Mn 2p XPS spectra of the initial MnO octahedrons, Janus MnO_x-Ag and MnO_x-AgI NPs.

Sample	Mn^{2+}	Mn^{3+}	Mn^{4+}
Peak position / eV	640.8	641.6	643.8
MnO	100	/	/
MnOx-Ag	37.5	50.9	11.6
MnOx-AgI	24	66	10

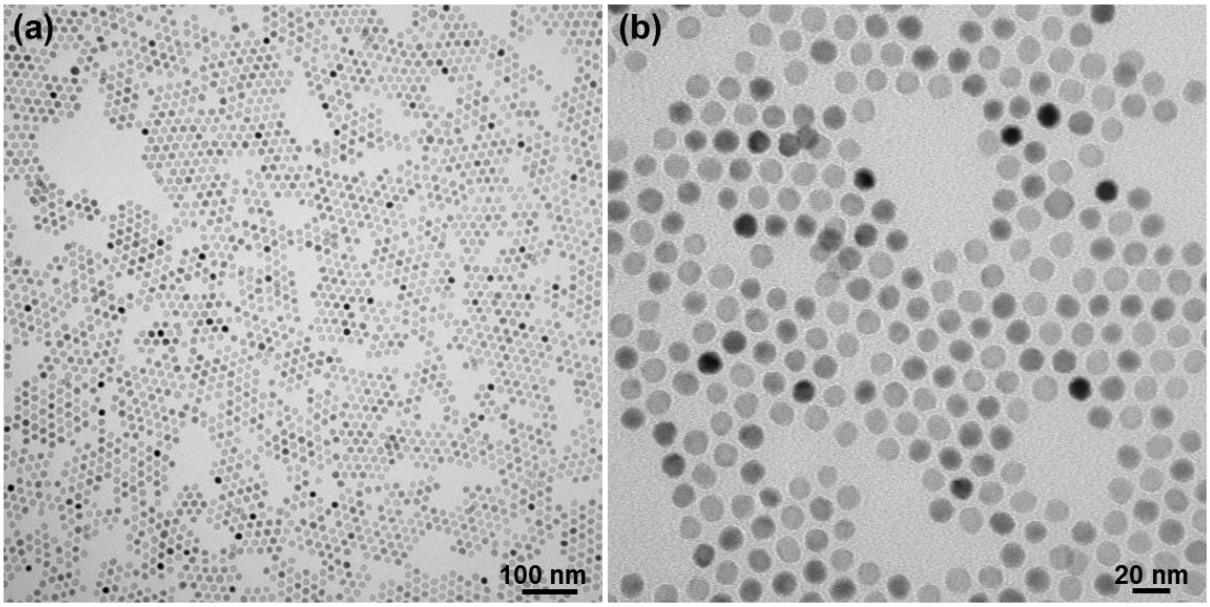

Figure S1. TEM images of the primary MnO octahedra showing the uniformity structures of MnO octahedrons.

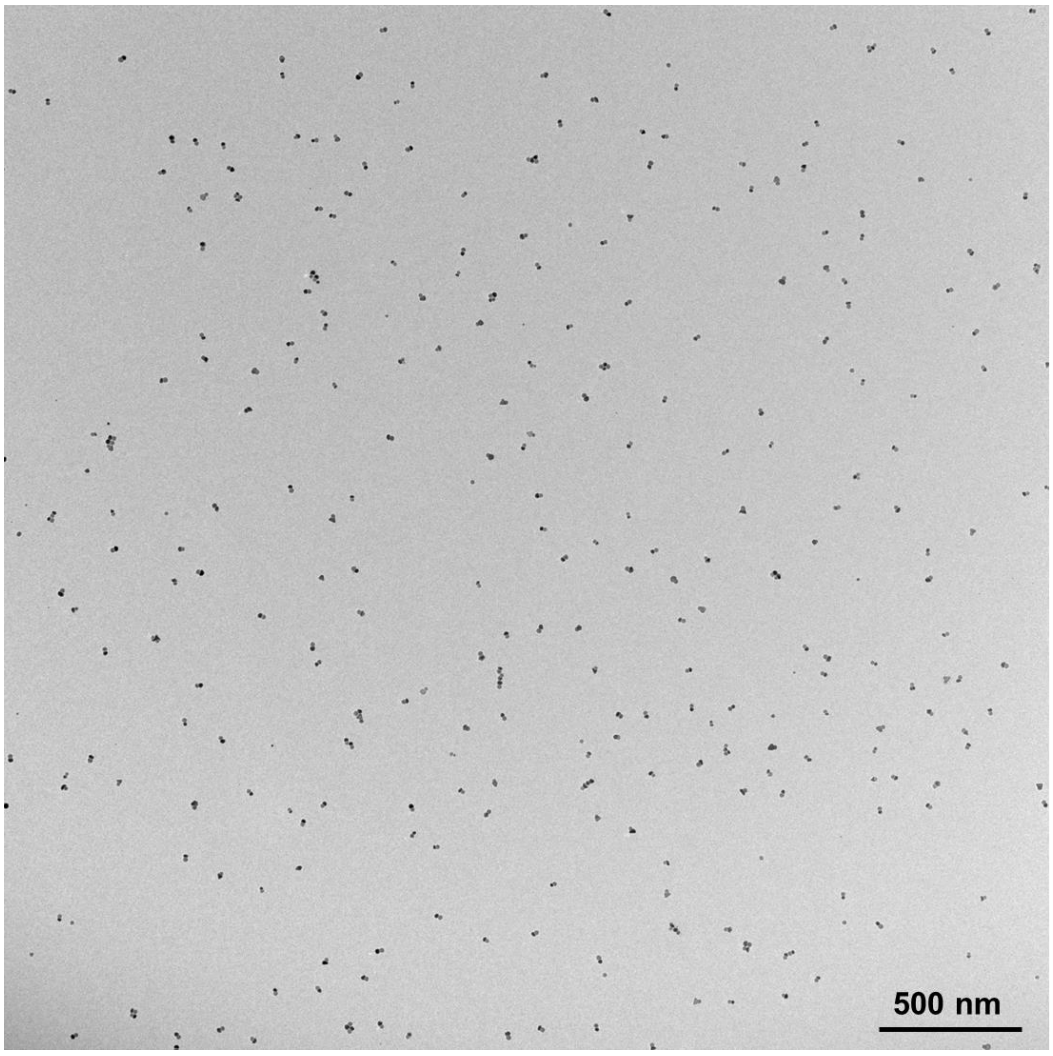

Figure S2. Low-magnification TEM image of the Janus-type MnO_x-Ag NPs.

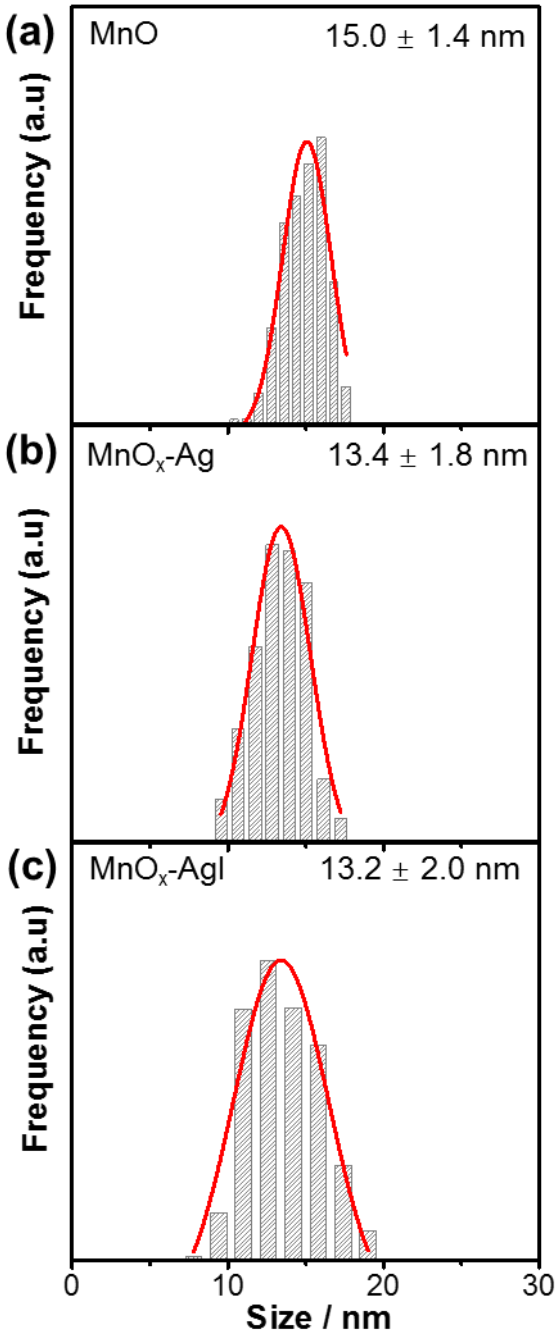

Figure S3. Size distributions of the MnO domain in (a) MnO octahedron, (b) Janus-type MnO_x-Ag NPs, and (c) Janus-type MnO_x-AgI NPs, measured from their low-magnification TEM images.

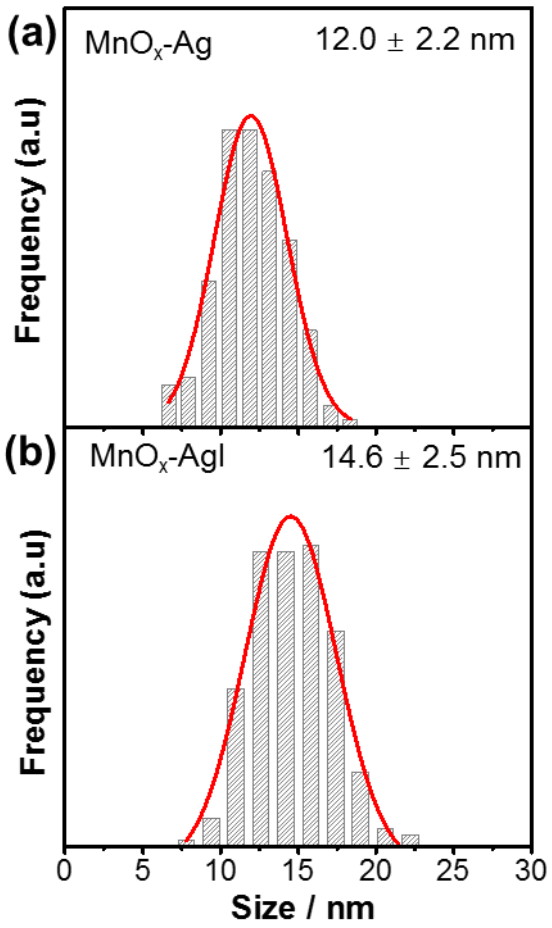

Figure S4. Size distributions of (a) the Ag domain in the Janus-type MnO_x-Ag NPs, and (b) the AgI domain in the Janus-type MnO_x-AgI NPs, measured from their low-magnification TEM images.

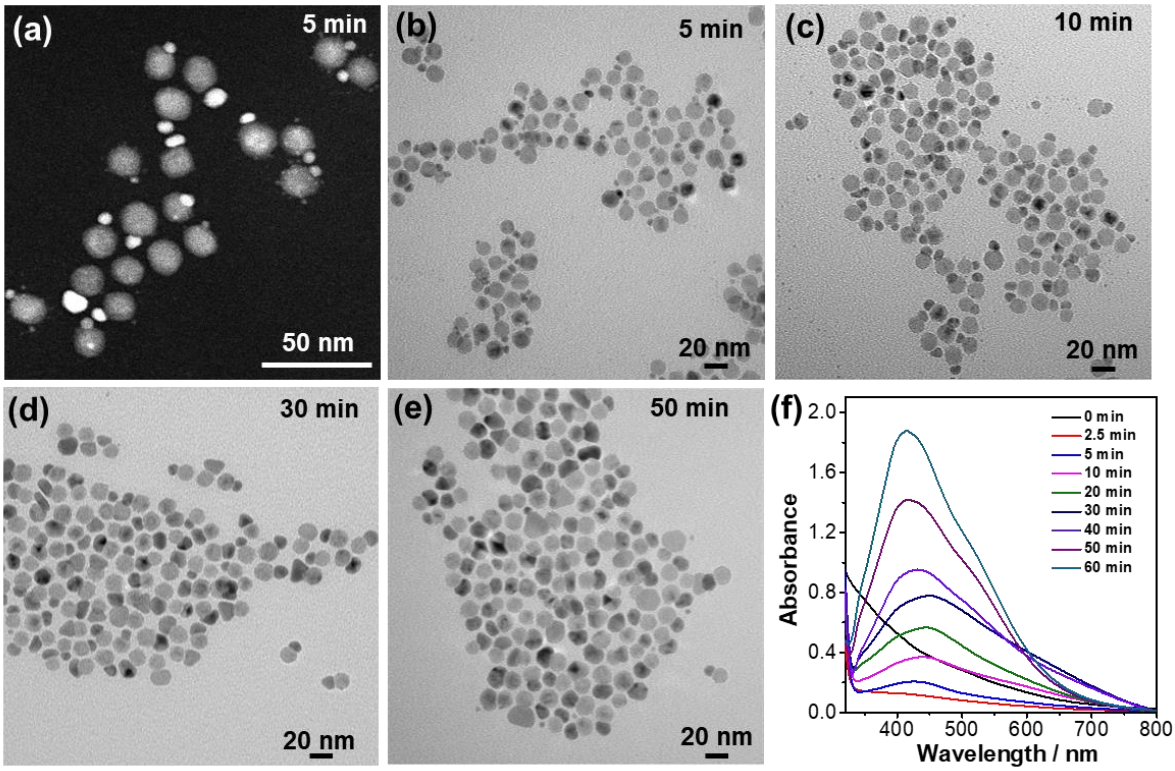

Figure S5. Evolution of the Janus-type MnO_x-Ag NPs obtained at different growth stages of nanocrystals. TEM images of the intermediates after (a–b) 5 min, (c) 10 min, (d) 30 min, (e) 50 min of the reaction, respectively. (f) The corresponding UV spectra of the intermediates as a function of the reaction time.

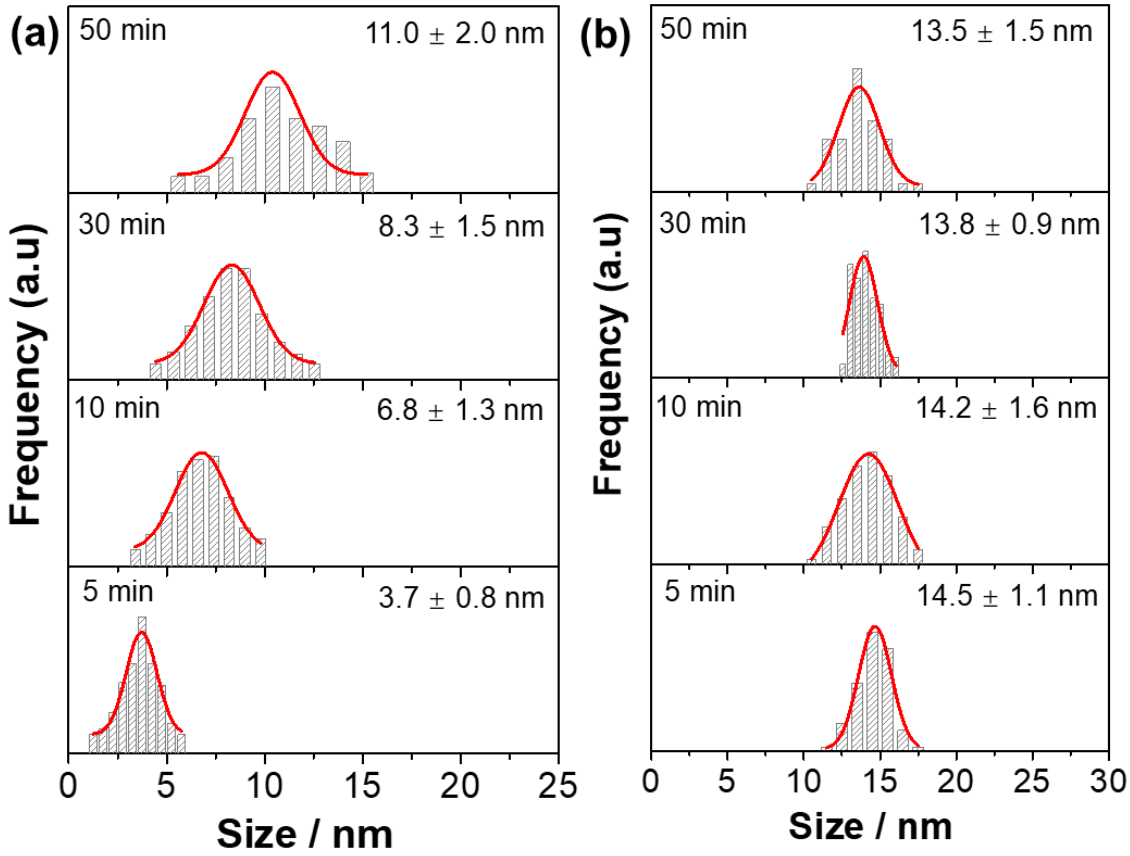

Figure S6. Size distributions of (a) Ag domains and (b) MnO_x domains in the reaction intermediates of Janus-type MnO_x-Ag after 5 min, 10 min, 30 min, 50 min of the typical reaction, respectively.

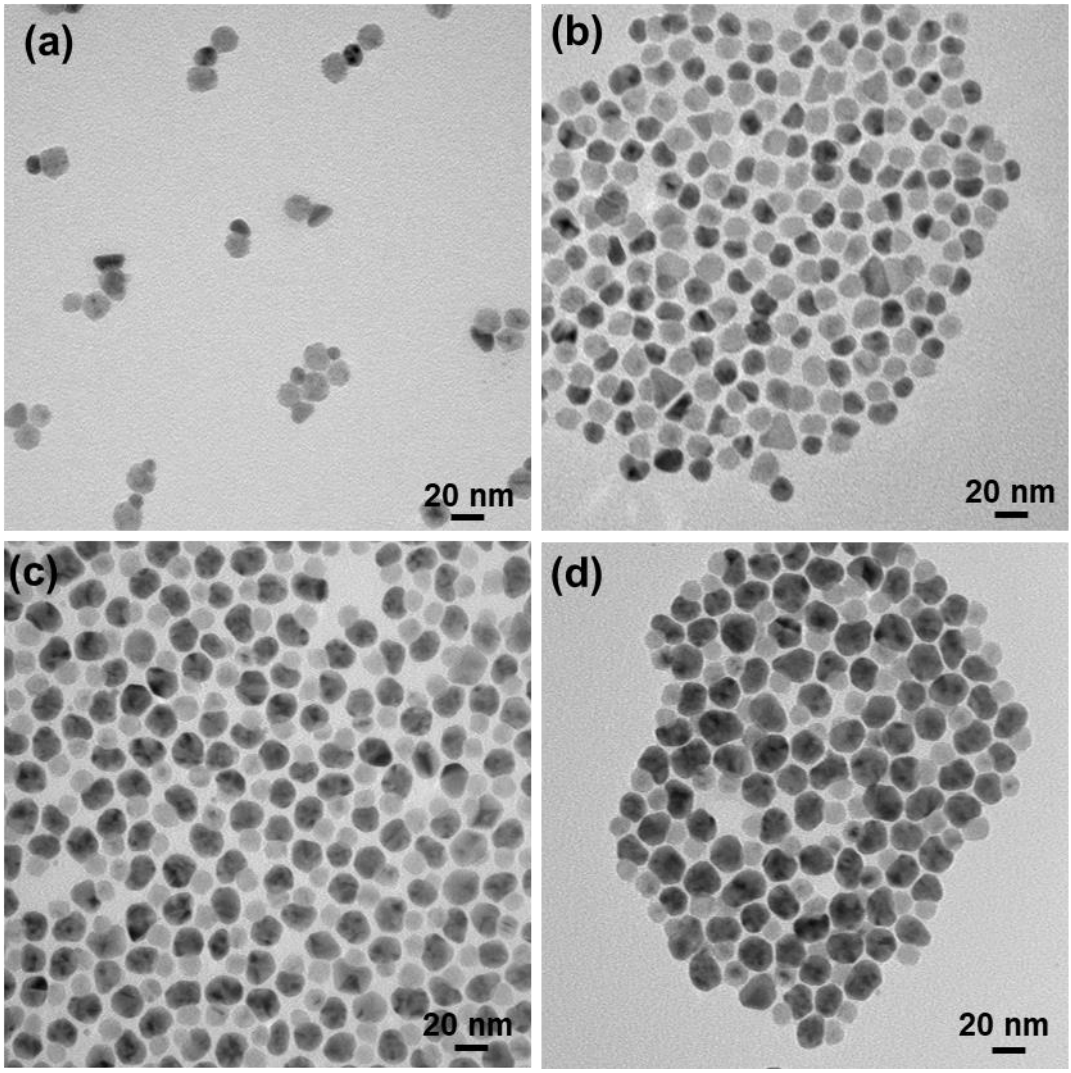

Figure S7. TEM images of the Janus MnO_x-Ag with different size of Ag domain obtained from a typical synthesis at different feed amount of $AgNO_3$ (50 mg/mL): (a) 500 μL, (b) 1 mL, (c) 1.5 mL, and 2 mL. The corresponding mole ratio of $AgNO_3$ to MnO for a-d is 0.5, 1, 1.5 and 2, respectively. The other reaction conditions were same.

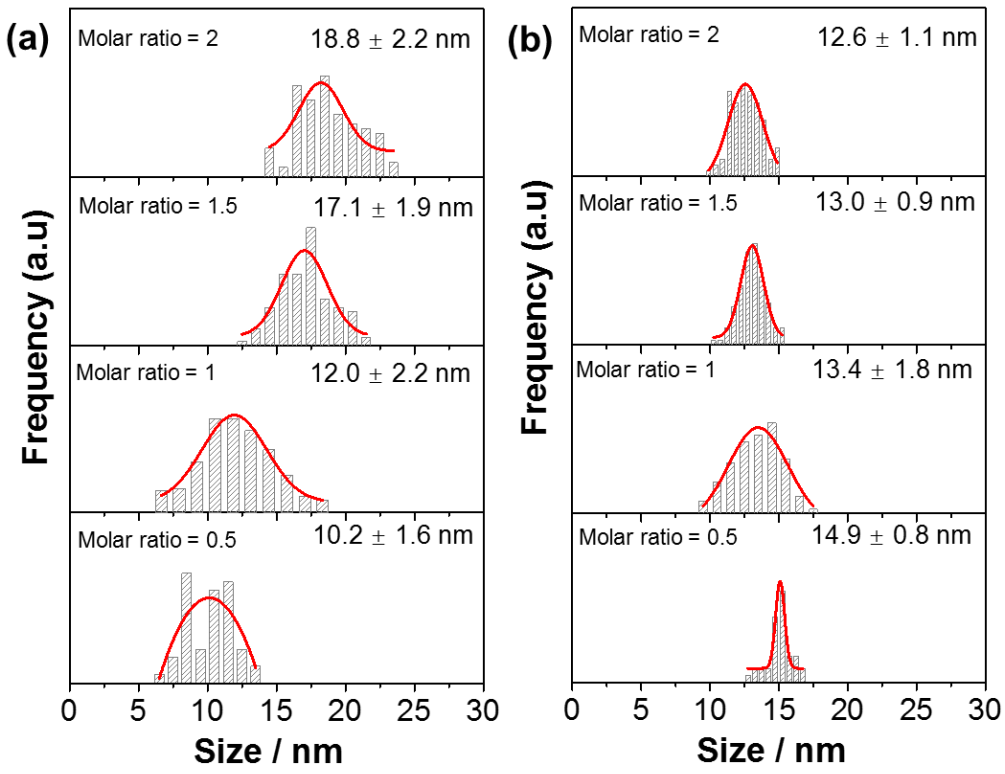

Figure S8. Size distribution of (a) Ag domain and (b) MnO octahedron from the corresponded TEM images in Figure S5. From bottom to up of the histogram, the molar ratio of $AgNO_3$ to MnO is 0.5, 1, 1.5 and 2, respectively.

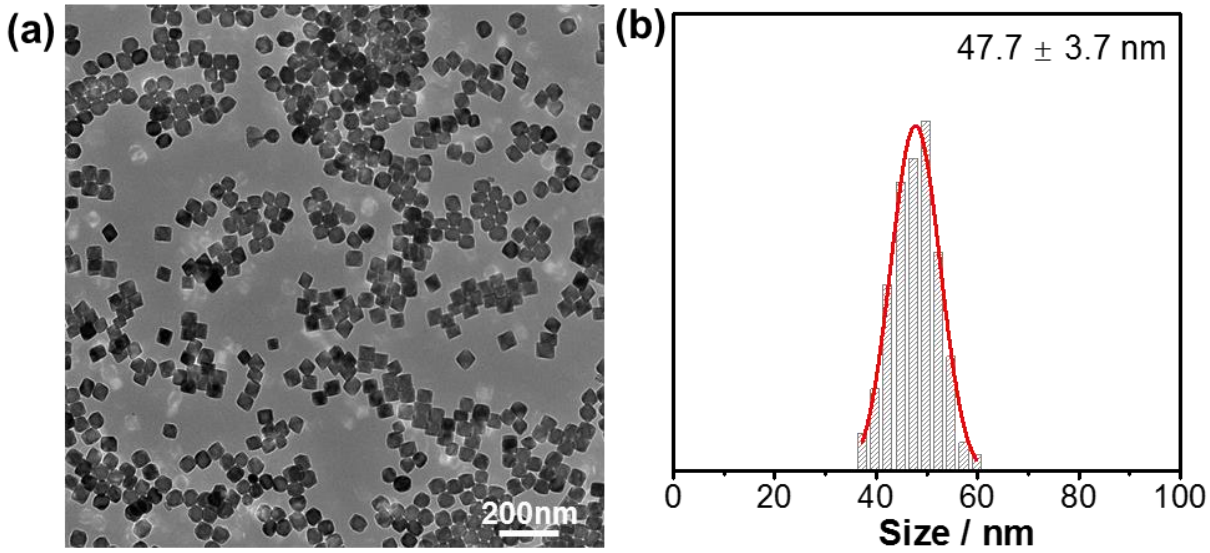

Figure S9. (a) TEM image and (b) corresponding size distribution of the MnO octahedron obtained by reducing heating rate.

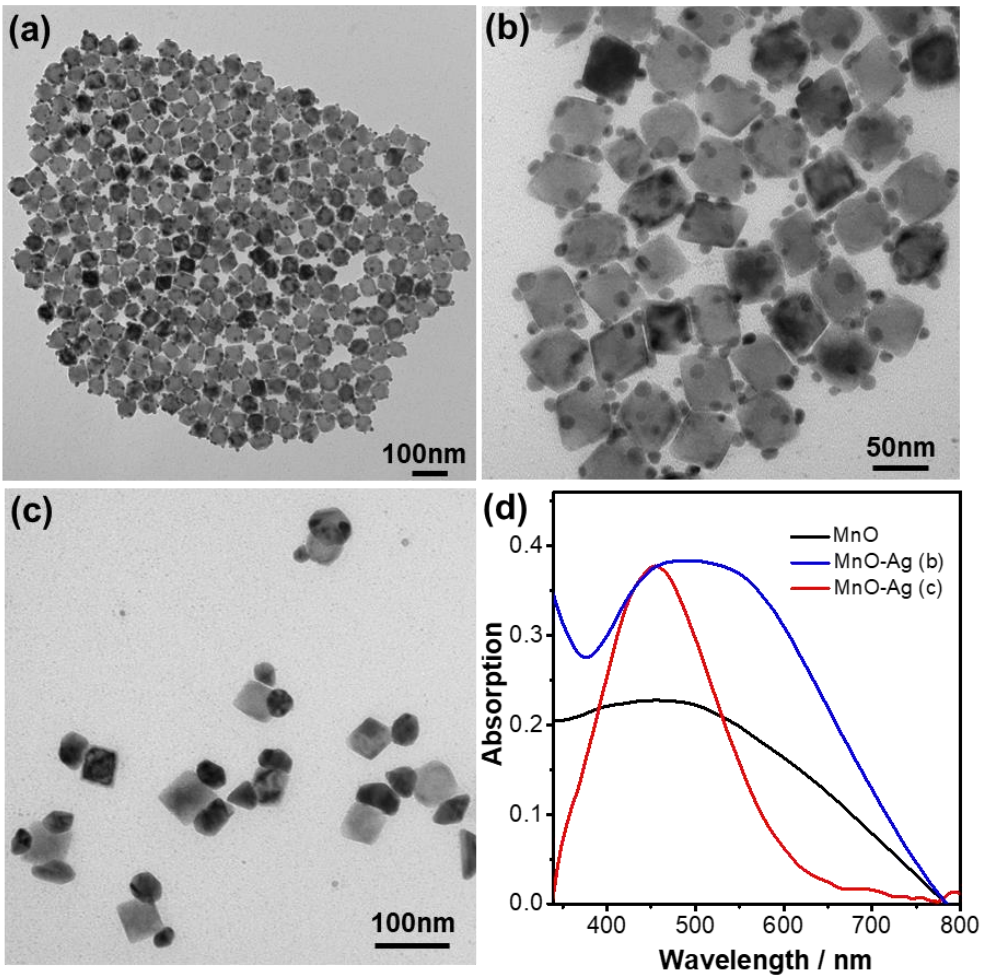

Figure S10. (a) TEM images of MnO_x-Ag nanostructure with different morphology grown on the ~ 48 nm MnO by adjusting the molar ratio of $AgNO_3$ to MnO. (a–b) 0.25, (c) 1. (d) Corresponding UV spectra of ~ 48 nm MnO and MnO_x-Ag with different morphology.

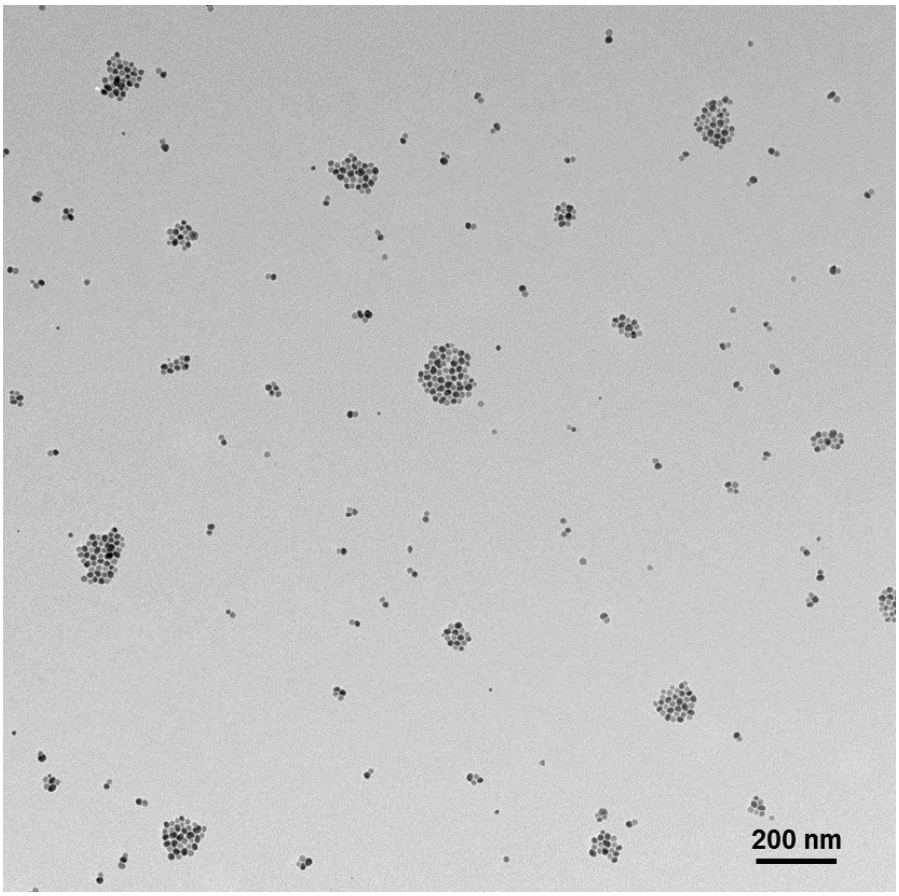

Figure S11. Low magnification TEM image of Janus-type MnO_x-AgI NPs.

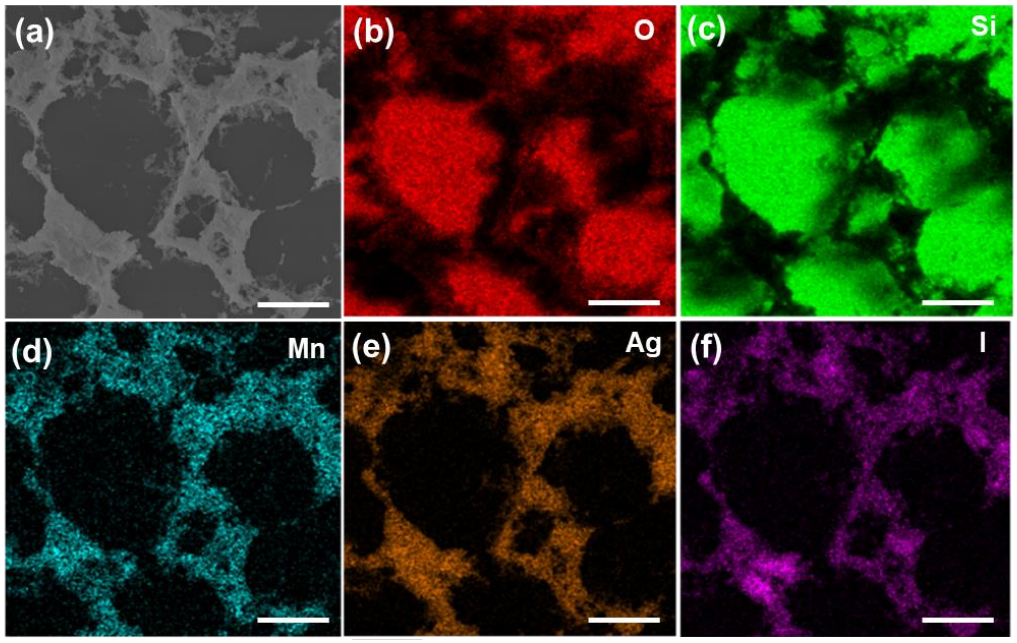

Figure S12. (a) Low magnification SEM image and EDX mapping of Janus-type MnO_x-AgI exhibiting the homogeneous distribution of (b) O, (c) Si, (d) Mn, (e) Ag and (f) I.

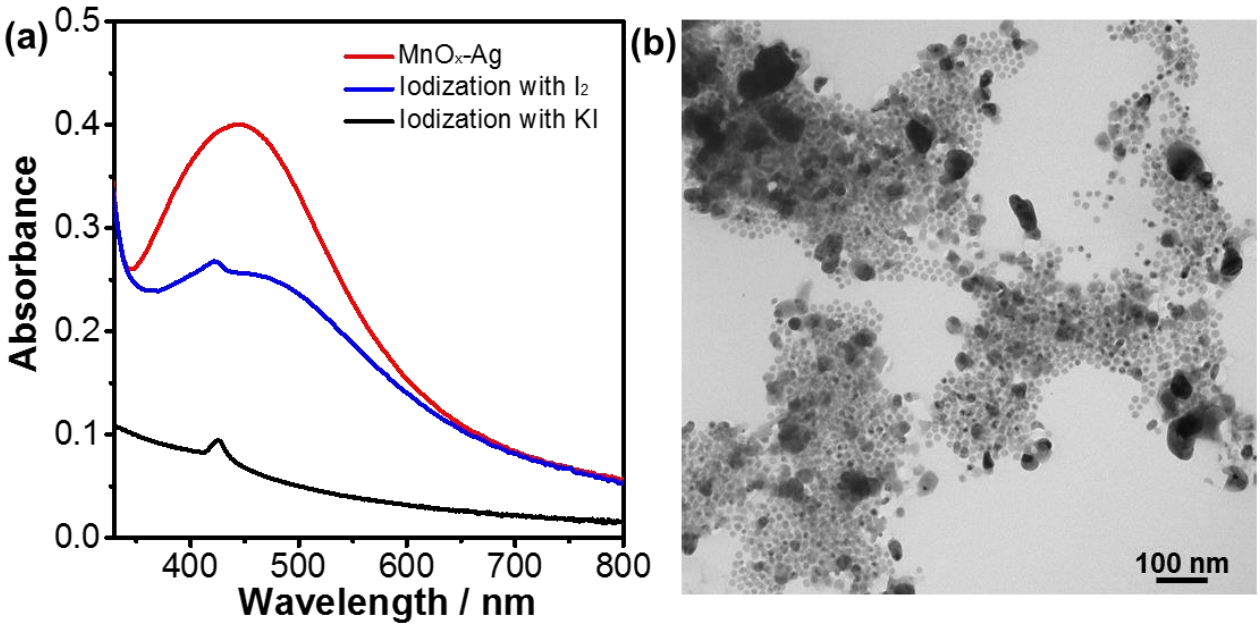

Figure S13. (a) The UV vis spectra of original Janus-type MnO_x-Ag NPs (red line) and MnO_x-Ag after iodizing with I_2 (blue line) and KI (black line). (b) The typical TEM image of Janus-type MnO_x-Ag after iodizing with I_2. The nanostructures were disrupted due to the iodization.

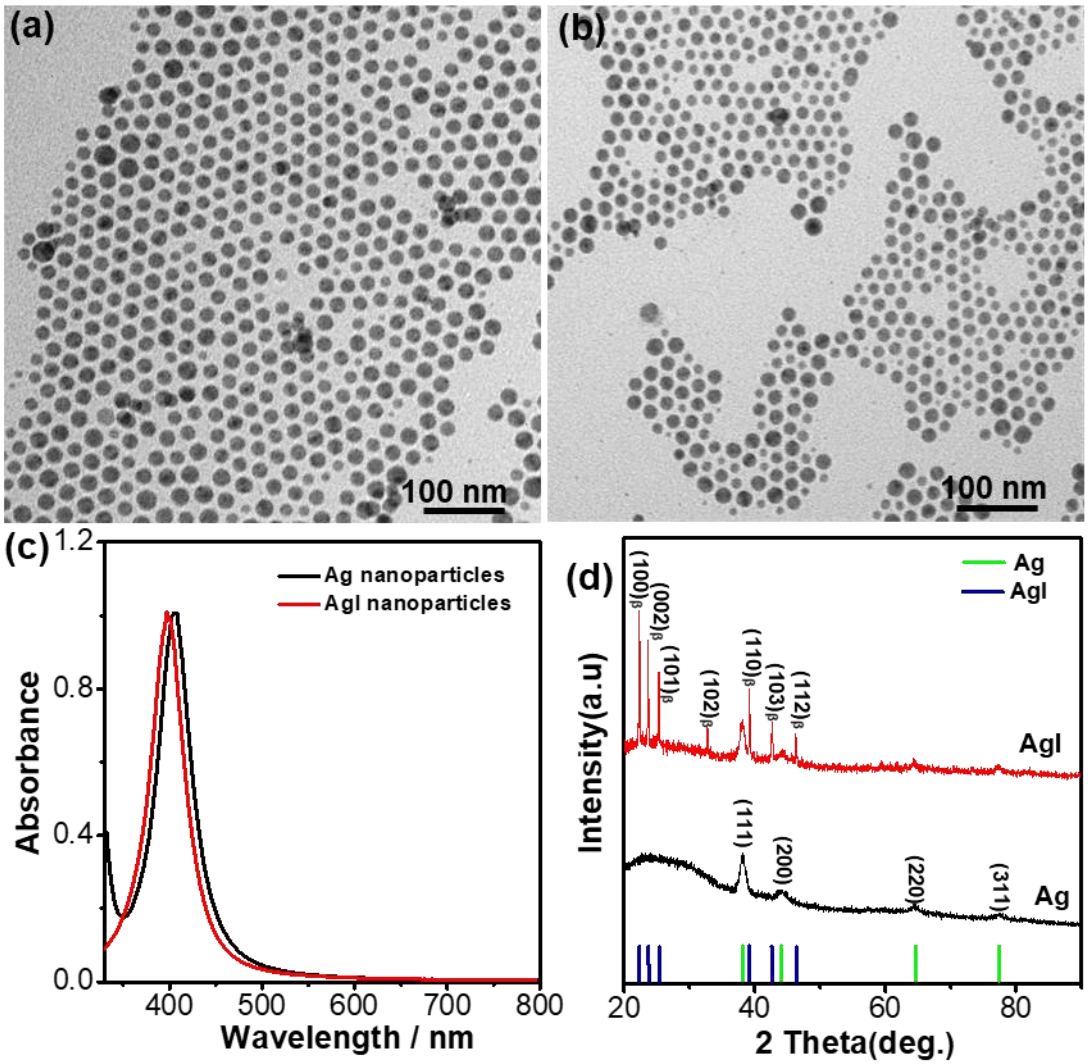

Figure S14. TEM images of (a) Ag and (b) AgI NPs. (c) The UV spectra of Ag NPs before and after iodization with iodomethane. (d) XRD patterns of Ag and AgI NPs. Standard positions for Ag and AgI are indicated by vertical lines at the bottom.

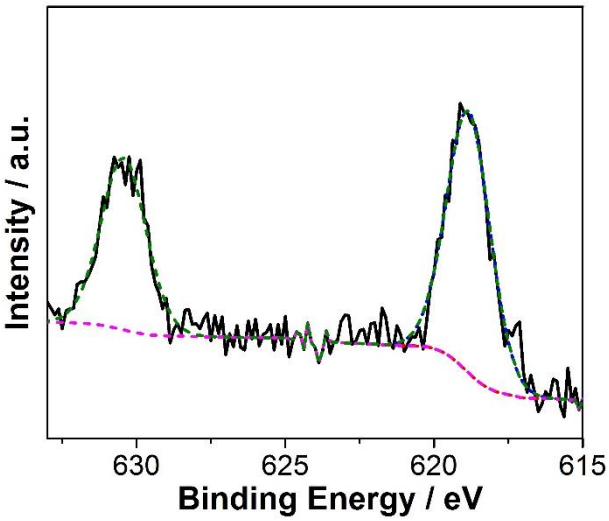

Figure S15. The I 3s deconvoluted results of X-ray photoelectron spectra of Janus-type MnO_x–AgI NPs.

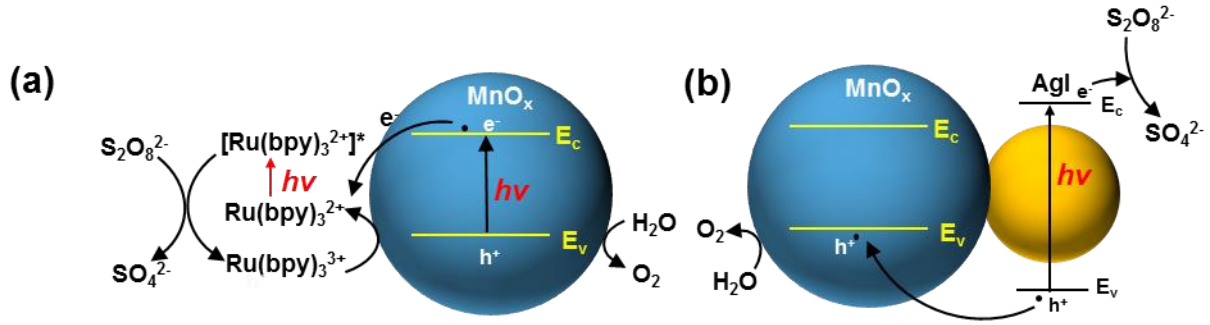

Figure S16. Reaction mechanism of photocatalytic water oxidation using (a) MnO_x using a $Ru(bpy)_3^{2+}/S_2O_8^{2-}$ system and (b) Janus-type MnO_x–AgI NPs without $Ru(bpy)_3^{2+}$.

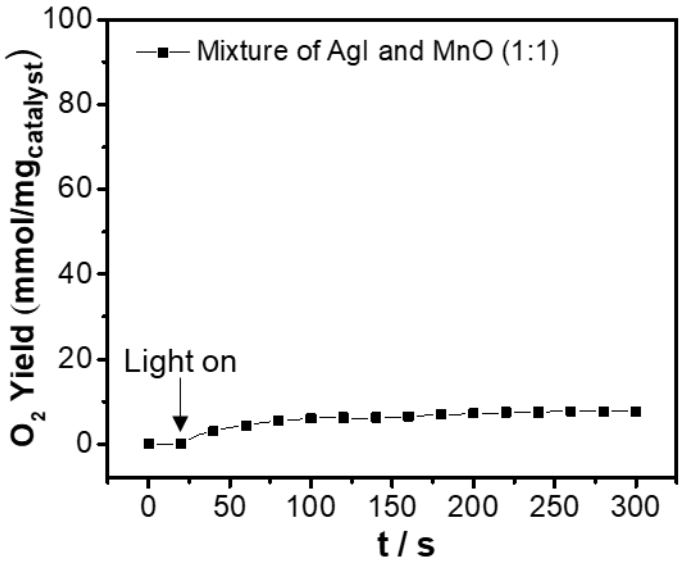

Figure S17. Dissolved oxygen evolution profiles of mixture of AgI and MnO in molar ratio of 1 to1 for the photochemical water oxidation without $Ru(bpy)_3Cl_2$. Photocatalytic conditions: 4 mg of catalysts, 13 mM $Na_2S_2O_8$, and 68 mM Na_2SO_4 in 15 mL of H_2O.

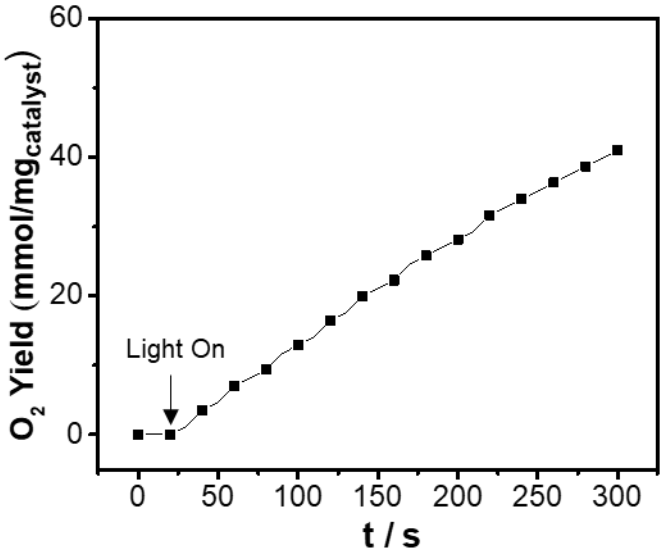

Figure S18. Dissolved oxygen evolution profiles of Janus-type MnO_x-AgI NPs for the photochemical water oxidation without buffer. Photocatalytic conditions: 4 mg of catalysts, 13 mM $Na_2S_2O_8$, and 68 mM Na_2SO_4 in 15 mL of H_2O.

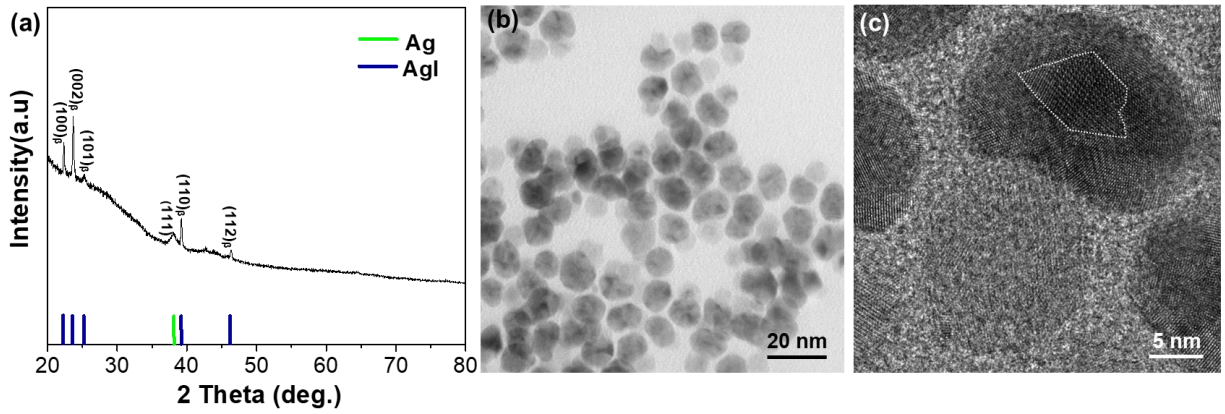

Figure S19. (a) Powder XRD pattern, (b) a TEM and (c) HR-TEM image of Janus-type MnO_x-AgI NPs recovered after five cycles for visible light driven WORs.

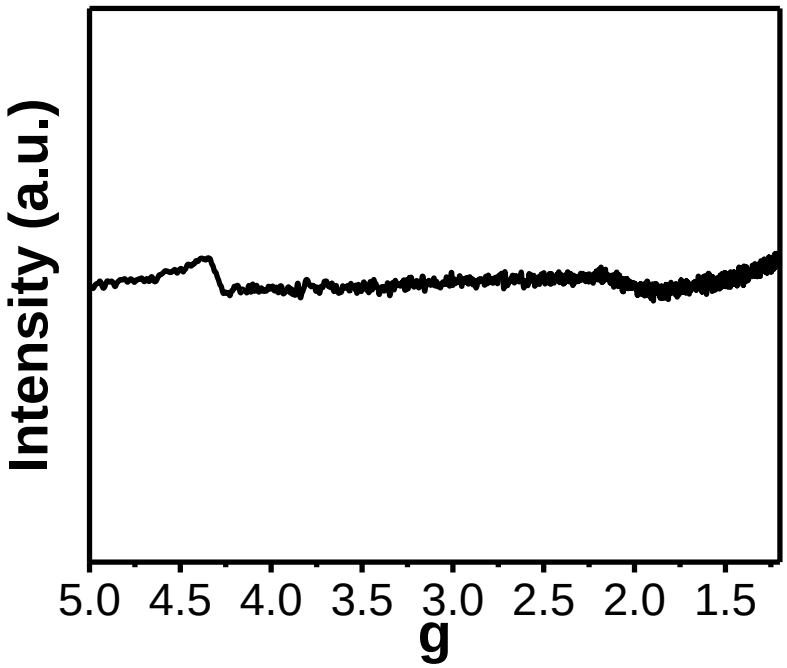

Figure S20. Perpendicular mode EPR spectra of MnOx–AgI after stability test.